

High-resolution velocity-map-imaging photoelectron spectroscopy of the O⁻ photodetachment fine-structure transitions

S. J. Cavanagh, S. T. Gibson, M. N. Gale, C. J. Dedman, E. H. Roberts, and B. R. Lewis

Research School of Physical Sciences and Engineering, The Australian National University, Canberra ACT 0200, Australia

(Received 11 July 2007; revised manuscript received 20 September 2007; published 19 November 2007)

A high-resolution photoelectron velocity-map-imaging study is reported for the photodetachment of the atomic oxygen anion at 532 nm, where five of the six possible spin-orbit fine-structure transitions have been resolved. A resolution of $\Delta E/E=0.38\%$ was achieved. Within the experimental uncertainty, each of the fine-structure transitions has the same anisotropy, the averaged $\beta=-0.89(1)$ consistent with previous, fine-structure-unresolved, experimental and theoretical determinations.

DOI: [10.1103/PhysRevA.76.052708](https://doi.org/10.1103/PhysRevA.76.052708)

PACS number(s): 32.80.Gc

I. INTRODUCTION

Since the pioneering experiment of Chandler and Houston in 1987 [1], charged-particle imaging experiments have progressed to a point where they are becoming equivalent, or even superior, to conventional electro- and magnetostatic techniques, especially in terms of efficiency and energy resolution for the collection and analysis of charged particles from gas-phase targets. Initially, the resolution obtainable from imaging experiments was limited, due to the finite extent of the interaction volume for the process under study. It was realized in 1997 [2] that, by using an appropriate electrostatic-lens configuration, this limitation could be overcome, leading to the velocity-map imaging (VMI) technique. These imaging techniques rely on producing 2D circular images of the 3D charged-particle distribution, where the radial extent of the image is proportional to particle velocity, and the intensity distribution around the outer edge is indicative of the angular distribution. However, one limitation of particle imaging techniques lies in the extraction of usable data from the images. When cylindrical symmetry of the process leading to the charged particle can be ensured, the reconstruction of the 3D velocity distribution from the 2D projected data can be carried out [2], e.g., through the use of an inverse-Abel transformation as described by Hansen and Law [3]. Alternatives to this direct mathematical transformation are the basis-set expansion (BASEX) technique of Dribinski *et al.* [4], and the iterative approach of Vrakking [5]. A comparative review of inversion techniques has been performed by Eppink *et al.* [6]. However, when dealing with large image sizes, these alternative methods can be cumbersome due to the very large amounts of physical computer memory and processing time needed to perform the inversion.

The technique of slicing, introduced in 2001 [7–9], does not work in general for the detection of photoelectrons, given the extremely fast arrival times due to their small mass. Slicing has been shown to work well for the detection of moderate to heavy ions, under the correct experimental conditions. Only for specific cases can slicing methods be applied to photoelectron detection, as has been done by Baguegard *et al.* [10] for the separation of threshold- and finite-energy electrons.

One of the main advantages of VMI for the detection of photoelectrons is the simultaneous collection of the photo-

electron spectra and photoelectron angular distributions. However, until now the relative energy resolutions reported for photoelectron spectra from imaging experiments has been limited to $\Delta E/E \gtrsim 2.0\%$ [11,12]. With this level of resolution, features such as the spin-orbit structure of light atomic ions and rotational transitions in light molecular ions will only be resolved if the kinetic energy of the photoelectrons (eKE) is quite low. Imaging of very low energy electrons is, of course, extremely difficult and fraught with problems, such as perturbations due to electric and magnetic fields and space-charge effects due to ion-electron and electron-electron interactions. Only for photodetachment from heavy ions would fine-structure transitions become visible for typical finite photoelectron energies. However, there is much physics and chemistry to be gleaned from fine-structure transitions, e.g., the causes for deviations from the statistical expectations for the branching ratios, and the possible detection of relativistic effects from the spin-orbit component dependence of the angular distributions, through the asymmetry parameter, β . To be able to observe fine-structure transitions using VMI at finite photoelectron energies would be a considerable advance. One target of interest is the atomic oxygen anion, O⁻, which has a spin-orbit splitting of ~ 22 meV [13] between the $^2P_{3/2}$ and $^2P_{1/2}$ states. Photodetachment from ground-state O⁻ gives rise to six possible subtransitions,

$$\text{O}^{-}(^2P_{3/2,1/2}) + h\nu \rightarrow \text{O}(^3P_{2,1,0}) + e^{-}. \quad (1)$$

To resolve these fine-structure transitions using VMI would require an energy resolution of $\Delta E/E \leq 1.0\%$.

The spectroscopic study of O⁻ dates back as far the 1930s [14] and has mainly focused on establishing a precise value for the electron affinity, EA. However, it was not until the mid 1980s that an accurate determination of the EA and spin-orbit splitting of the anion was made, using threshold photodetachment spectroscopy [15]. Since the 1970s, threshold photodetachment techniques have been well developed. However, the lack of suitable laser dyes for the O⁻ threshold region restricted progress. Within the past decade, new measurements performed using laser photodetachment microscopy have established the definitive EA of $11,784.676(7) \text{ cm}^{-1}$ ($1.4611135(12) \text{ eV}$) [13,16]. In addition, the laser photodetachment microscopy value for the

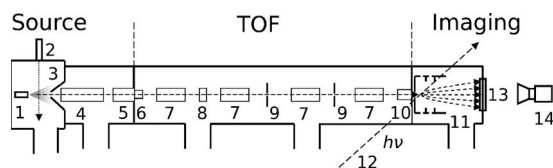


FIG. 1. Schematic of fast anion-beam VMI spectrometer, segmented into three regions, as indicated. (1) Pulsed supersonic jet and pulsed discharge. (2) Electron gun. (3) Molecular beam skimmer. (4) Ion electrostatic acceleration optics. (5) Gating, potential rereferencing, and bunching unit. (6) and (8) Electrostatic ion-beam deflectors. (7) Ion-beam Einzel lens. (9) Stainless-steel apertures. (10) Potential rereferencing switch, electrostatic ion-beam deflectors and potential barrier. (11) VMI lens. (12) 532-nm linearly-polarized laser beam. (13) MCP (multichannel plate) and phosphor detector. (14) CCD (change-coupled device). See text for details.

spin-orbit splitting of the negative ion is in good agreement with estimates produced by threshold photodetachment, leading to the accepted value of $177.084(14) \text{ cm}^{-1}$ [13,17].

None of the techniques used to accurately establish the EA and spin-orbit splitting can be used to extract angular distributions. Previously, most angular distribution measurements have not resolved the fine-structure transitions, providing a mean β value for the six combined transitions [18,19]. Only the measurements of Breyer *et al.* [20], at the wavelengths of 488 and 514.5 nm, have yielded resolved β values, for three of the six fine-structure transitions. For these measurements, they employed an electrostatic hemispherical analyzer with radius 50 mm and 0.5 mm slit widths, operated at a pass energy of 0.6 eV and with narrow angular acceptance, achieving an overall energy resolution of 4.7 meV. Since their measurements [20], there have been no further reported experimental data on fine-structure-resolved angular distributions for O^- photodetachment.

In this paper, we report the results of the first VMI study of photodetachment from O^- . Despite the use of a fast anion beam, and a large interaction region, a photoelectron energy resolution of $\Delta E/E=0.38\%$ has been achieved, enabling the full resolution of five of the six fine-structure transitions, and the determination of β parameters for each resolved transition.

II. EXPERIMENT

The experimental apparatus is shown in Fig. 1, with an expanded view of the VMI lens and its associated potential switch and barrier shown in Fig. 2. Essentially, the apparatus produces a collimated beam of mass-selected negative ions, which can then be interrogated by a laser beam, subsequently producing photoelectrons. The photodetached electrons are then imaged onto a multichannel-plate phosphor detector using a modified VMI lens.

Oxygen anions are produced by passing pure oxygen gas through a pulsed nozzle (General Valve Series 9) at a stagnation pressure of 2.0 atmospheres and then supersonically expanding it through a pulsed discharge. The base pressure of the source region is typically 10^{-7} mbar and rises to 5×10^{-6} – 10^{-5} mbar when the pulsed valve is operating. The

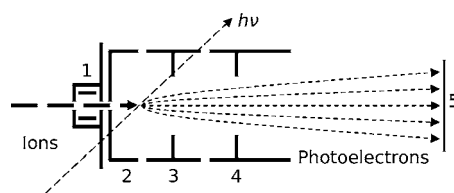


FIG. 2. Schematic of VMI lens (not to scale). The ions enter along the lens axis, their corresponding velocity component not affecting the photoelectron energy resolution. (1) Potential rereferencing switch, electrostatic deflectors, and ion beam potential barrier. (2) VMI repeller element. (3) VMI extractor element. (4) VMI grounded element. (5) MCP, phosphor, and CCD detector.

pulsed discharge is similar in design to that of Osborn *et al.* [21], except for the replacement of the cylindrical stainless steel electrodes by four sharpened pins that only just protrude into the gas stream midway along the device's length. As in the Osborn design, the discharge requires seeding by an electron gun in order to stabilize the discharge cycle. With this modification, more ions are emitted from the discharge, with no visible effect on their thermal motion and narrow energy distribution.

All negative ions are then extracted, accelerated to 500 eV, and focused into an ion gating, bunching, and potential rereferencing unit. This unit gates the ion packet, rereferences the ions from acceleration to ground potential, and finally bunches the ion packet to optimize the number density in the interaction region [22]. Following this process, the ion packet passes along a 2-m mass time-of-flight (TOF) tube containing four unipotential (Einzel) lenses, two apertures and three electrostatic deflectors, for focusing, collimation, and steering of the ion beam. With ion-beam energies of 500 eV, and in combination with the ion gating, bunching and potential rereferencing unit, mass resolving powers ($m/\Delta m$) of 450–500 are achieved.

After the TOF section, the ion beam enters the VMI lens coaxially. A second fast potential switch is used to rereference the ion packet from the ground potential of the TOF to the repeller plate potential. This minimizes adverse effects on the ion beam trajectories, bunching properties, and flux. A potential barrier, placed between the second potential switch and the repeller plate of the imaging lens, is typically operated at 20% above the ion-beam energy so that no ions reach the imaging lens when the potential switch is grounded. The barrier is then switched in unison with the potential switch to the switch (and repeller) potential. When switched in this way, the barrier acts as a mass discriminator, only allowing the one mass of interest into the imaging lens. Positioning of the ion beam in the interaction region is enhanced by a set of electrostatic deflectors located within the second potential switch. If these deflectors are switched in unison with the potential switch body, no undesired effects are imparted to the ion-beam trajectories.

Within the VMI lens, the ion beam is crossed by the detachment laser beam, generated using a Continuum Powerlite 9010 Nd:YAG laser operated at its second harmonic, 532 nm. For these measurements, the laser was operated at 10 Hz repetition rate, with pulse energies of 1–10 mJ. To

ensure a very high degree of polarization that is parallel to the MCP detector face, the laser beam was passed through a $1/2$ -wave plate and high-quality Glan-Laser polarizer. As our VMI lens can accommodate a large interaction volume, discussed below, the need to focus the laser beam to a small spot size is negated. Instead, we use a Galilean telescope arrangement to produce a parallel beam of 2 mm in diameter, reduced from the laser's 8-mm diameter. This minimizes the effect of multiphoton processes due to large electric-field gradients.

The VMI lens design, the technical aspects of which are described in detail elsewhere [23], is a substantially modified version of the original design due to Eppink and Parker [2]. The motivation for this modification was to (1) achieve a resolution superior to that of any other VMI lens design, (2) accommodate a fast ion beam with beam energies of hundreds to thousands of eV, and (3) increase the interaction-region volume from $<500 \mu\text{m}^3$ to at least 2mm^3 , without affecting the ultimate resolution. To this end, we have used charged-particle electrostatic theory to scale and alter the lens dimensions of the Eppink and Parker design, while adding cylindrical rings between each of the lens apertures. Through these design aspects, the field gradients in the interaction region are relaxed and the field lines along the imaging lens become straighter and less tight. The modelled resolutions that should be attainable from our system, using Simion 6.0 [24], are $\Delta E/E=0.2\%$ ($\Delta v/v=0.1\%$), for a 2mm^3 interaction region imaged onto a 75-mm diameter detector. As was pointed out above, the ion beam is coaxial with the imaging lens. The main motivation for this was to overcome the inherent axial velocity spread imparted to the ion beam by the bunching process, which would be reflected in the photoelectron spectra if the ion beam were to cross perpendicular to the imaging lens axis. To bunch a 500-eV O^- beam from 80 mm in length to 2 mm over a 2-m length requires a bunching voltage of $\sim 35 \text{V}$. If in a perpendicular arrangement, the energy spread imparted to the photoelectron spectra would be on the order of 10 meV. This would completely dominate the performance of our spectrometer. However, the coaxial arrangement is not completely free from the influence of ion-beam properties. In this arrangement, not only is the position of the interaction region critical, as is the case for all imaging experiments, but also the ion-beam divergence. In most cases, it is easier to minimize divergence than it is to produce a highly monoenergetic ion beam.

Photoelectrons are imaged onto a position-sensitive detector, consisting of a pair of image-quality microchannel plates (MCPs), a P47 phosphor screen, and a 1.9 Megapixel CCD camera. The imaging detector is situated at the end of a TOF tube, 800 mm from the interaction region. Due to this long TOF tube, and the fact that we are imaging photoelectrons, screening of magnetic fields is essential. This is done through a combination of μ -metal shielding and three pairs of 2.5-m orthogonal Helmholtz coils. Given that the detector is in the path of the ion beam and any neutral species resulting from the photodetachment, the MCP gain is gated using a purpose-built fast HV pulser to coincide with the arrival of the photoelectrons. Images from the phosphor are captured by a 1600×1200 pixel monochrome CCD camera (SCOR-20SO) from Point Grey Research. Each camera frame is transferred

to and processed by a PC, in real time at 10 Hz, using computer algorithms designed to centroid each event to subpixel accuracy and then store the XY coordinates. This entire process can be achieved easily with event rates from tens to hundreds of photoelectrons per frame. The number of events required to achieve statistically significant data governs accumulation times.

An inverse Abel transformation is employed in order to extract the 3D distribution from the 2D image. However, as with any photoelectron spectrometer, the electron trajectories from the interaction region to the detector can be perturbed easily and, as a result, the nested circular images may exhibit some small distortions. In order to achieve a successful inversion, these distortions should be removed. Ideally, the spectrometer should be arranged so as to minimize them, but in reality this is achieved rarely. Therefore, an image circularization procedure has been implemented to remove these distortions. The circularization, or morphing, is carried out by radially scaling the image, with the scaling factor determined by the comparison of adjacent radial-slice intensity profiles. The image is then processed using the inverse-Abel transformation procedure described by Hansen and Law [3].

The laser-ion beam overlap position, although not as critical in its effect on the resolving power as discussed by others [25], still requires optimization. With the imaging detector on the TOF optical axis, defined by apertures, placement of the ion packet in the optimal location within the VMI lens can be achieved by locating the ion-cloud position on the imaging detector, comparing this with simulations, and then optimizing the position using the electrostatic deflectors. This positioning can then be achieved independently of the laser-beam propagation. By using this comparative technique, virtually all properties of the ion beam can be extracted. Given the independent positioning of the ion beam, the spatial and temporal overlap of the laser and ion beams can be achieved by maximizing the photoelectron signal. The combination of these methods allows for the precise positioning of the interaction region at its optimum location within the imaging lens.

The only other parameter to be set is the focusing condition of the imaging lens itself, determined by the extractor-to-repeller voltage ratio. The repeller voltage is chosen so that electrons with maximum kinetic energy strike the MCP at or near its maximum radius. With this established, measurements are taken for a range of extractor potentials, with the resolving power of the imaging system determined for each voltage ratio. The optimum repeller-to-extractor voltage ratio can then be determined easily. With our optimum voltage ratios, and a stable ion beam, effective photoelectron energy resolutions of 3.3 meV were achieved. When taking into account the absolute kinetic energy of the electrons, 0.86898 eV for the $^3P_2 \leftarrow ^2P_{3/2}$ transition at 532 nm, our eKE resolution is $\Delta E/E=0.38\%$ ($\Delta v/v=0.19\%$). This level of performance was maintained easily for 12 h or more, and on consecutive days.

III. RESULTS AND DISCUSSION

Figures 3(a)–3(d) show the accumulated photoelectron velocity-map image, inverted image, and respective slice in-

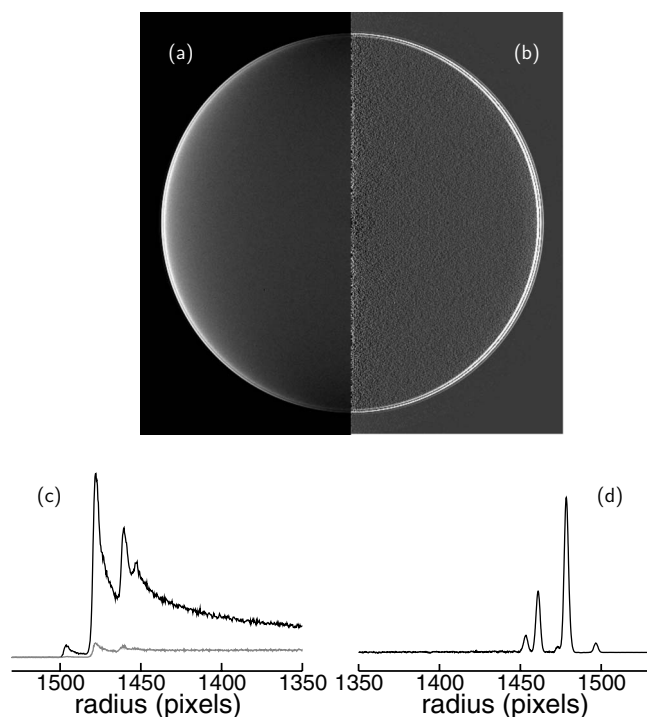


FIG. 3. A compilation of data collected for photodetachment of O^- at 532 nm where the laser electric vector is in the vertical direction. (a) Raw (non-processed) photoelectron image, 4800×3600 pixel, generated by binning the centroided electron events. (b) Corresponding inverse-Abel transformed image. (c) 10° slice from raw photoelectron image (a) in the horizontal (upper plot) and vertical (lower plot) directions. (d) Total photoelectron intensity after transformation and integration along lines of constant radius. Even within the raw image, 4 of the 6 fine-structure transitions are visible with the fifth a clear inflection on the right-hand side of the most intense peak in (c). The inverse Abel transformation results in accumulation of noise towards the centre of the image, which is evidenced by a slight increase in the background ripple for the smaller radii in the slice profile (d).

tensity profiles, for photodetachment of O^- at 532 nm. The VM image is obtained by binning each camera-image (1600×1200) electron event into a $3 \times$ larger (4800×3600) image, a necessary step in order to extract the structure. The size of one binned pixel is approximately equivalent to one MCP pore, the limit for the certainty of the XY position for any photoelectron event. Most of the intensity is accumulated in concentric circles, corresponding to the ~ 0.87 -eV eKE, with a propensity for the electrons to be distributed in the horizontal direction in Fig. 3(a). Two features of the raw and inverted images should be noted: (1) That the electric-field vector is in the vertical direction with respect to the images and (2) the lack of any discernible background within the image (best observed beyond the outermost ring) and the photoelectron spectrum. This latter aspect is of significance, since any background component of an image is highly unlikely to be linear across a large MCP. In this case, linear background subtraction (e.g., [26]) would distort not only the photoelectron spectrum, but also the angular distribution. Achieving this level of signal-to-noise was described previously in [27] and will not be discussed further here.

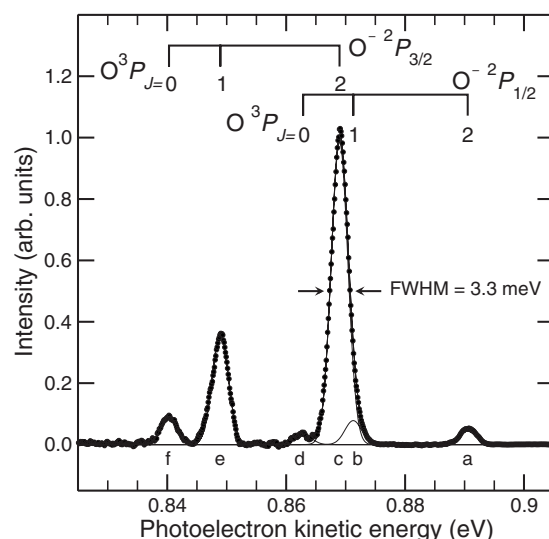


FIG. 4. Relative photoelectron spectrum for a 500-eV O^- beam (with significant axial velocity spread), photodetached by 532-nm, linearly-polarized photons. The experimental spectrum (circles) is well fitted by a sum of individual Gaussian functions (lines). The FWHM resolution, taken from the $O(^3P_2) \leftarrow O(^2P_{3/2})$ transition, is $\Delta E = 3.3$ meV ($\Delta E/E = 0.38\%$). The low intensities for the transition originating from the $O(^2P_{1/2})$ anion state are a characteristic of the anion source. Labeling of the transitions, a–f, follows the notation of [29].

Five of the six possible fine-structure transitions have been resolved in the photoelectron spectrum, with at least four identifiable within the raw image. These transitions are best identified from a 10° circular wedge taken directly from the raw image, as in Fig. 3(c). This detailed level of structure is apparent, even though the smallest separation between any two identifiable transitions is ~ 6 meV. The FWHM for each transition is ~ 1 camera pixel, emphasizing the requirement for sub-pixel centroiding, even for a 1600×1200 -pixel camera image.

Within the dipole approximation, the angular distribution of the photoelectrons for randomly-orientated targets with linearly-polarized light is given by [28]

$$\frac{d\sigma(E)}{d\Omega} = \frac{\sigma_{\text{total}}(E)}{4\pi} [1 + \beta(E)P_2(\cos \theta)], \quad (2)$$

where E is the kinetic energy of the photoelectron, θ is the angle between the light electric vector and the momentum vector of the photoelectron, σ_{total} is the total cross section for photodetachment, and β is the anisotropy (asymmetry) parameter, which contains all of the dynamics of the photodetachment process. Following energy calibration, described below, a relative σ_{total} is evaluated from the VM image of Fig. 3(b), by integration over θ of the image intensity. This process is equivalent to integration of Eq. (2) over θ ($0 - \pi$), and an azimuthal angle ϕ ($0 - 2\pi$), due to the cylindrical symmetry of the electron distribution imposed by the polarized laser beam. The resultant photoelectron spectrum (relative photodetachment cross section), is shown in Fig. 4. Here the remarkable resolving power of our implementation

TABLE I. Fine-structure intensity ratios for the $O(^3P_{J'}) \leftarrow O(^2P_{J''})$ transitions at 532 nm, compared with other experimental and theoretical results.

$\frac{J'' \rightarrow J'_1}{J'' \rightarrow J'_2}$	Ref. [20]		Ref. [31] ^a	This work ^b	
	514.5 nm	488.0 nm	364.0 nm	532.0 nm	Theory ^c
$\frac{3/2 \rightarrow 1}{3/2 \rightarrow 2}$	0.368(11)	0.365(14)	0.41	0.365(2)	0.36
$\frac{3/2 \rightarrow 0}{3/2 \rightarrow 2}$	0.084(4)	0.084(6)	0.10	0.093(2)	0.08
$\frac{1/2 \rightarrow 1}{1/2 \rightarrow 2}$	1.98(20)	2.07(25)	1.3	1.80 ^d	1.80
$\frac{1/2 \rightarrow 0}{1/2 \rightarrow 2}$	0.85(8)	0.85(11)	0.5	0.81(7)	0.80

^aEstimated from Fig. 1 of Ref. [31] (uncertainties unknown).

^bUncertainties are 1σ values returned by least-squares fitting procedure.

^cFrom Eq. 13 of Ref. [37]; Eq. 3 of this work.

^dValue fixed in the fit.

of the VMI lens is revealed. Fine-structure transitions are well isolated, with five of the six possible transitions resolved.

The energy scale of the photoelectron spectrum was determined by taking the accurate EA value of Blondel *et al.* [16], calculating the corresponding photoelectron energy for detachment at 532 nm, squaring the radius, and then normalizing to the appropriate transition. Nonlinearities in the energy scale, determined by comparisons using the known spectroscopic data on O [30] and O^- [13], are estimated to be $<0.1\%$. As pointed out by [2], the application of an imaging lens requires an additional scaling factor to the flat-field approximation for the charged-particle trajectories. In our case, deviations from the flat field were $<0.5\%$ (values given later). No other manipulation of the images or spectrum was carried out.

The spectrum of Fig. 4 is well described by the sum of six Gaussian functions, the parameters of which were determined by least-squares fitting to the experimental data. Energies for the peaks labeled (b) and (d) were constrained in the fit to the expected O-fine-structure splitting from peak (a), and the amplitude of (b) was constrained to be $1.8\times$ the amplitude of (a) (see Sec. III A). The least-squares fit yielded a FWHM of 3.3 meV ($\Delta E/E=0.38\%$) for the strongest transition. This width \approx one camera pixel and 1.8 MCP pores. The fitted peaks (a)–(f) are displaced by $-3.3, 0, 0, 0, 3.2, 4.8 \text{ cm}^{-1}$, respectively, relative to the expected spectroscopic positions. The fitted O^- spin-orbit splitting from our data, $178.8(3.8) \text{ cm}^{-1}$, is consistent with the precise values of $177.13(5) \text{ cm}^{-1}$, from laser threshold photodetachment spectroscopy [15], and $177.084(14) \text{ cm}^{-1}$, from photodetachment microscopy [16]. As the position of any photoelectron event cannot be determined to better than one MCP pore, this corresponds to an inherent energy uncertainty of $\sim 0.6 \text{ meV}$ ($\sim 5 \text{ cm}^{-1}$), and an inherent angular resolution better than 0.1° , both referenced to the outer ring in the photoelectron image.

A. Transition intensities

The fitted intensity ratios listed in Table I, displayed so as to make them independent of ion-source conditions, are in good agreement with the previous measurements of Breyer *et al.* [20], despite their measurements being undertaken at the shorter wavelengths of 514.5 nm and 488.0 nm. The relative intensities of Ervin *et al.* [31], taken with an instrumental resolution of 6 meV FWHM at a wavelength of 364 nm, i.e., 1.0–1.1 eV higher in photon energy, are also shown in Table I. Their intensity ratios for the resolved transitions arising from the $^2P_{3/2}$ anion state are not too dissimilar from the present values and those of Breyer *et al.* [20], but their ratios from the $^2P_{1/2}$ state appear to differ. However, these latter ratios, derived from mostly unresolved transitions, have undocumented, and probably large, uncertainties and should be treated with caution.

The O^- photodetachment process described by Eq. (1) involves the detachment of a p electron, with the production of outgoing s and d waves. The analogous process in S^- has been treated theoretically near threshold, where s waves are expected to dominate [32], by Rau and Fano [33]. Adapting an idea due to Lineberger and Woodward [34], they [33] considered the final state as an ($e+\text{atom}$) complex created by the absorption of a photon by the LS -coupled anion, with coupling changing from LS , when the electron is close to the atom, to JJ , as the electron recedes to infinity. Under these conditions, Rau [35] showed that the relative intensities of the fine-structure transitions are given by a purely geometric factor $Q(J', J'')$, where $J'' (= \frac{1}{2}, \frac{3}{2})$ and $J' (= 0, 1, 2)$ refer to the anion and neutral atom, respectively, which does not involve the full dynamics of the photodetachment process.

In the general case of photoionization and photodetachment, as shown, e.g., by Dill *et al.* [36] and Pan and Starace [37], the former of whom introduce the concept of angular-momentum transfer, the geometric and dynamical factors become entangled in the fine-structure cross sections, which

involve incoherent sums over the relevant partial waves, leading to complications in the determination of the branching ratios. However, under the approximation of term-independent dynamical amplitudes, typical of the central-potential model, factorization is possible again, with the geometric factor applicable to our particular case of s - and d -wave photodetachment in O^- being given by [37]

$$Q(J', J'') = [J'] \sum_{\lambda} [\lambda] \begin{Bmatrix} 1 & \frac{1}{2} & \lambda \\ \frac{1}{2} & J' & 1 \end{Bmatrix}^2 \begin{Bmatrix} 1 & \frac{1}{2} & \lambda \\ J'' & 1 & 1 \end{Bmatrix}^2, \quad (3)$$

where λ is a summation index, $[\lambda] = 2\lambda + 1$, and $[J'] = 2J' + 1$. Evaluation of the $6j$ symbols for each J'' , J' leads to the theoretical intensity ratios listed in the last column of Table I, which are, in fact, *identical* to the threshold s -wave ratios of Rau [35]. We note here that alternative formulations of the photodetachment process, where the $LS \rightarrow JJ$ recoupling is performed first, and the photon is then absorbed, provide equivalent results [29,38,39].

The theoretical branching ratios in Table I are in excellent agreement with the present experimental values and those of Breyer *et al.* [20]. The present experiment results in an $eKE \approx 0.87$ eV, i.e., well away from threshold, where, as will be seen in Sec. III B, both s and d waves are involved in the photodetachment process, with the s - and d -wave intensities adding incoherently [36,37]. Evidently, the experimental results support the factorizability of the geometric factor from the photodetachment cross sections, and the corresponding constancy of the fine-structure branching ratios for O^- photodetachment from threshold to an eKE of at least 1.1 eV. It would be of interest to provide further experimental tests of the range of validity of Eq. (3) and its underlying approximations by extending the present high-resolution study to a wider range of photon energies.

B. Photoelectron angular distributions

The angular distribution evident in the VM image of Fig. 1(a) is clearly nonisotropic, with intensity tending to a minimum in the direction of the laser polarization. The photoelectron intensities [40] for the five resolved fine-structure transitions are shown in Fig. 5, plotted as a function of $P_2(\cos \theta)$, with the intensities normalized to $I[P_2(\cos \theta) = 0] = 1$. According to Eq. (2), such plots should be linear, with slopes yielding the β parameters. All of the transitions, apart from the strongest $O(^3P_2) \leftarrow O^-(^2P_{3/2})$, demonstrate uniform linear dependences for the intensity variation with $P_2(\cos \theta)$, and the fitted β values are the same, to within the combined experimental uncertainties.

The nonlinear dependence seen in the $O(^3P_2) \leftarrow O^-(^2P_{3/2})$ transition intensity beyond an angle of $P_2(\cos \theta) = 0.4$ in Fig. 5(c) is due to an experimental artifact. Since (1) the collection efficiency of the VMI technique is 100%, (2) no background subtraction has been necessary, and (3) no detector or laser-beam electric vector rotation, as is normally used in conventional angular-distribution measurements, is required for the VMI technique, the most likely cause of the intensity loss is an MCP detector-gain-related issue. As discussed by Wu and co-workers [41], corrections

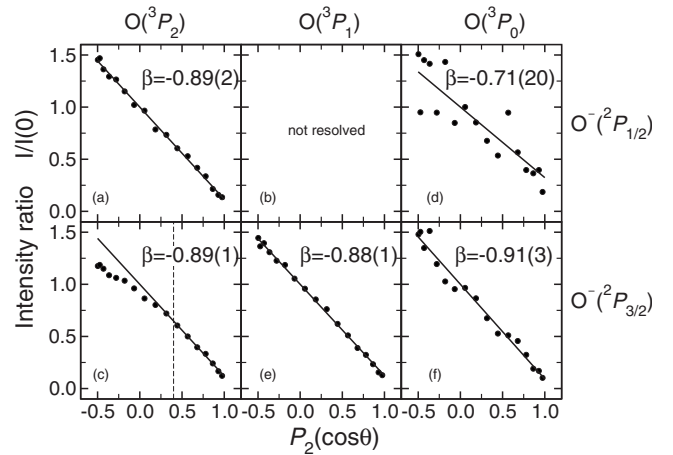


FIG. 5. Photoelectron angular distributions for the $O(^3P_j) \leftarrow O^-(^2P_{j'})$ transitions, with intensities evaluated for 5° slices of the VM image (circles), together with the corresponding linear regressions (solid lines), with slopes yielding the β values. The labels (a)–(f) follow those in Fig. 4. The $O(^3P_0) \leftarrow O^-(^2P_{1/2})$ transition (b) is not resolved. The $O(^3P_2) \leftarrow O^-(^2P_{3/2})$ transition (c), which is the most intense, exhibits nonlinear behavior for $P_2 < 0.4$ (dotted line), i.e., for $\theta \geq 40^\circ$, which is indicative of saturation of some pores of the MCP detector (see text). For this transition β has been determined from the range $P_2(\cos \theta) > 0.4$.

to images due to spatial sensitivity or gain irregularities may still be required, even though careful implementation of event counting should negate them. These losses are usually attributed to the inherently imperfect spatial gain profile across an MCP, whether new or old. However, a mechanism that can also result in spatial gain irregularities is very high flux densities of charged particles. This is particularly true when a detection threshold level has been set in order to distinguish between real impacting charged-particle events and the inherent background noise from the detectors, i.e., readout noise from a CCD.

For pulsed-mode imaging experiments, this loss of gain, or saturation, can be of particular importance, resulting in many impacts highly concentrated in one particular region of an MCP, all of which arrive in a brief time period. Particles at the leading edge of the packet can easily drain charge from a localized area of the MCP, diminishing the amplification for immediately subsequent events. This effect can distort seriously both the relative intensities and the angular distributions. As it is induced by the charged-particle flux density, trying to determine the gain profile by the application of a uniform signal cross the MCP will not succeed. The only avenues open for its removal are to either lower the flux density or the detection-threshold levels. Both of these solutions have their shortcomings, e.g., increasing data-collection times, or increasing uncertainty in the XY coordinate of each event. An alternative approach is to determine where in the image the saturation is occurring and then to only use data extracted from the image outside of this region. This procedure will work for angular distributions, but not for the extraction of relative transition intensities, due to the β dependence of the cross sections. If, however, the values of β for each transition can be obtained, a β -independent total pho-

TABLE II. Fine-structure-resolved β values for the $O(^3P_{J'}) \leftarrow O(^2P_{J''})$ transitions at 532 nm, compared with the results of Breyer *et al.* [20].

$J'' \rightarrow J'$	Ref. [20]		This work
	514.5 nm	488.0 nm	
$3/2 \rightarrow 2$	-0.923(8)	-0.912(16)	-0.89(1)
$3/2 \rightarrow 1$	-0.921(10)	-0.907(18)	-0.88(1)
$3/2 \rightarrow 0$			-0.91(3)
$1/2 \rightarrow 2$	-0.914(15)	-0.909(23)	-0.89(2)
$1/2 \rightarrow 1$			
$1/2 \rightarrow 0$			-0.71(20)

photoelectron spectrum can be extracted. It is this approach that has been used here.

The $^3P_2 \leftarrow ^2P_{3/2}$ transition constitutes by far the most intense transition within our image, with the feature spread over only 2–3 MCP pores, $\sim 100 \mu\text{m}$. This saturation effect can be easily seen in Fig. 5(c), and occurs only for $\theta \geq 40^\circ$. Figure 5(e) shows the angular distribution for the $^3P_1 \leftarrow ^2P_{3/2}$ transition, which is the second most intense feature, where the signal was spread over the same number of MCP pores, but without saturation. Therefore, the data extracted from the VMI image for the total photoelectron spectrum and hence relative transition intensities and the angular distribution for the $^3P_2 \leftarrow ^2P_{3/2}$ transition were taken from $P_2(\cos \theta) > 0.4$, while the angular distributions for the remaining transitions were taken from $0 - \pi/2$. It should be noted that, for the purposes of analysis, the four quadrants of the raw image were folded into one quadrant, after radially circularizing the VM image, in order to improve the statistics. This is possible due to the inherent symmetry of the photodetachment process and resultant image.

The β parameters obtained for each of the resolved fine-structure transitions are shown in Table II, compared with the only other fine-structure-resolved measurements, due to Breyer *et al.* [20]. As mentioned above, due to the very high degree of polarization of the laser beam and the lack of any discernible background within the photoelectron image, no correction terms taking into account the effects of laser depolarization and background were required for the present β determinations. Therefore, fitting of Eq. (2) to the data, plotted as intensity versus $P_2(\cos \theta)$, directly yielded β . This contrasts with all previous experimental determinations of β for O^- , where background and/or depolarization contributions were taken in account explicitly. The uncertainties in Table II are 1σ values returned by the least-squares fitting procedure, dominated by the statistical component, but also implicitly including any systematic component due to residual nonlinearity, caused, e.g., by saturation, as discussed above.

The values of β for each fine-structure transition in Table II are the same to within the combined uncertainties, taking into account that the low intensity of the $^3P_0 \leftarrow ^2P_{1/2}$ transition, and its location next to the most intense feature in the image, lead to a very large uncertainty in the corresponding β value, due to poor statistics. The relative lack of fine-

TABLE III. Fine-structure-averaged β values for the $O(^3P) \leftarrow O(^2P)$ transitions, compared with previous work.

λ (nm)	Ref. [19]	Ref. [18]	Ref. [20] ^a	This work ^a
458.2	-0.808(20)			
488.0	-0.876(18)	-0.885(15)	-0.911(16)	
514.5	-0.888(20)		-0.922(8)	
532.0				-0.89(1)
589.2	-0.881(32)			
727.6	-0.43(7)			

^aAn average of the fine-structure determinations, weighted according to transition intensity and uncertainty. The tabulated uncertainties correspond to those for the strongest fine-structure transition.

structure dependence in the β values is not unexpected, given the common angular-momentum values of the transitions, the narrow energy range spanning the transitions, the low photon energy used, and the low atomic number of the species studied, implying minimal relativistic effects. As discussed by Breyer *et al.* [20], relativistic effects should not be as important here as in the case of atomic photoionization, due to the different character of the final-state interactions.

Although the present β values agree with those of Breyer *et al.* [20] within the combined uncertainties, there is a small systematic shift to a less negative value, the reasons for which are unclear. The strengths of the present experimental technique include (1) a VMI system with a constant transmission function of 100% for the photoelectrons, (2) no need of corrections for finite acceptance angles, ion-beam velocity, or ion-beam divergence, and (3) negligible background. In support of the latter, no background can be seen beyond the outermost ring in our photoelectron image, and measurements performed under the same experimental conditions, but alternately with and without the ion and laser beams present, resulted in a background of only 1 part in 10^5 . The sole weakness in the present apparatus relates to the limiting detector saturation described in detail above. Although this is believed to have a negligible influence on the β values presented here, any such residual effect will indeed result in a less negative value.

Weighted fine-structure-averaged β values determined from the present fine-structure-resolved results, and those of Breyer *et al.* [20], are compared in Table III and Fig. 6 with other experimental results where the fine structure was unresolved [18,19]. From Fig. 6, although all experimental results are in quite good agreement, the β values of [20] lie systematically slightly lower than the dominant trend of the other results.

Also shown in Fig. 6 are the numerically calculated β -value curve of Cooper and Zare [28] for O^- photodetachment (solid curve) and model curves from Hanstorp *et al.* [19]. In the central-potential model, β for the photodetachment of an electron with initial orbital angular momentum l is given by the well-known Cooper-Zare formula [28], in terms of the dipole radial matrix elements $R_{l\pm 1}$ and phase shifts $\delta_{l\pm 1}$. Making simple assumptions regarding the energy dependences of $R_{l\pm 1}$, Hanstorp *et al.* [19] have parametrized this expression, yielding, in the case of O^- :

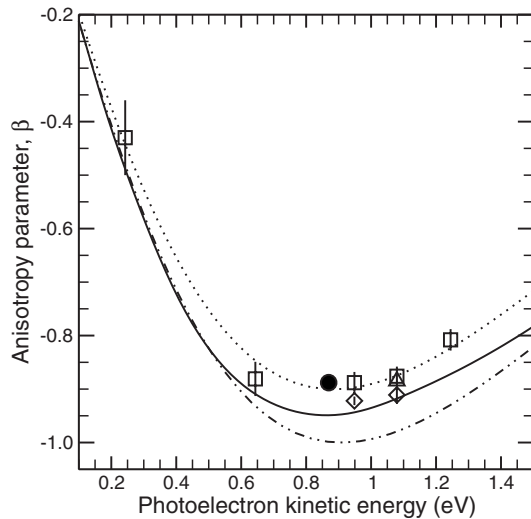


FIG. 6. Comparison of experimental and theoretical fine-structure-averaged β values for the $O(^3P) \leftarrow O(^2P)$ transition. Circle: This work. Diamond: Breyer *et al.* [20]. Triangle: Hall and Siegel [18]. Square: Hanstorp *et al.* [19]. Solid curve: Cooper and Zare [28] theory. Dot-dashed and dotted curves: Model of Hanstorp *et al.* [19], with $A_2=0.55 \text{ eV}^{-1}$ and $\cos(\delta_2 - \delta_0)=1.0$ and 0.925 , respectively. The present data and those of Breyer *et al.* are weighted averages with respect to transition intensity and uncertainty.

$$\beta(\epsilon) = \frac{2A_2^2\epsilon^2 - 4A_2\epsilon c}{1 + 2A_2^2\epsilon^2}, \quad (4)$$

where $c = \cos(\delta_2 - \delta_0)$ is the relative phase shift between the d and s outgoing waves, $A_2\epsilon = R_2/R_0$ is the ratio of the corresponding radial matrix elements, and ϵ is the photoelectron energy. For pure s -wave photodetachment, $A_2=0$, implying $\beta=0$, while for pure d -wave detachment, A_2 is very large and β tends to a value of $+1$. The depth of the minimum in this model for β is governed predominantly by the size of the phase shift c , while its position is largely dependent on A_2 . As noted by [19], if the values $A_2=0.55 \text{ eV}^{-1}$ and $c=0.96$ are used in Eq. (4), the curve generated is similar to that of [28], the solid line in Fig. 6, but with increasing deviation at higher eKE. The other two curves in Fig. 6 were generated using two different values for the phase shift, $c=1.0$ (dot-dashed curve) and 0.925 (dotted curve), but the same value for A_2 . A value of $c=1.0$ represents zero phase shift between the two outgoing partial waves. Our value for β , and the other fine-structure unresolved results [18,19], lie close to the dotted curve in Fig. 6, constructed using a phase difference of $\cos(\delta_2 - \delta_0)=0.925$. This suggests that there may be slightly more phase shift between the two partial waves than implied by the theory of [28].

Finally, we note that a recent calculation performed at 532 nm by Zatsarinny and Bartschat [42], using B -spline R -matrix methods [43], yielded the length and velocity results $\beta=-0.88$ and $\beta=-0.91$, respectively, a range broadly consistent with the comparable fine-structure-averaged experimental results in Table III. However, due to the difference between the length and velocity values, it is not pos-

sible to use these theoretical results to support any particular experimental result over another, since the small theoretical uncertainty is comparable to, or greater than, the experimental uncertainties.

IV. SUMMARY AND CONCLUSIONS

The relative photodetachment cross section for O^- at 532 nm has been measured using a high-resolution velocity-map-imaging spectrometer, enabling the extraction of intensity ratios and β parameters for five of the six fine-structure transitions. This was achieved through a new VMI lens design, despite using a fast O^- beam with a significant axial velocity distribution, and a large interaction volume. The energy resolution achieved, $\Delta E/E=0.38\%$, is the best yet obtained for any VMI experiment, both for ions and electrons. Only the ion slice imaging technique of Lipciuc *et al.* [44] has resulted in a similar resolution, but their result was obtained for the much heavier CD_3^+ ions and vastly smaller interaction volumes, the latter resulting from the tight focusing requirement for the two-color resonance-enhanced multiphoton-ionization process employed. We emphasize here that it is not only the VMI lens design [23] which is important in achieving our ultimate photoelectron energy resolution. For example, the careful control of ion-beam alignment and divergence, the maintenance of electrostatic-element voltage stability, and the minimization or elimination of contact potentials, and stray electric and magnetic fields, are essential. In addition, it is necessary to pay particular attention to the processes of data accumulation and analysis, including the performance and noise-sensitivity of the centroiding, image-circularization, and Abel-inversion algorithms. Beyond the issue of energy resolution, the simultaneous acquisition of photoelectron spectra and angular distributions inherent in the VMI technique, enhanced by 100% collection and near 100% detection efficiencies, have resulted in much more rapid data accumulation than possible using traditional methods. Thus, VMI is now a powerful method for the high-resolution study of photodetachment, particularly for radical anions at low number densities.

The present experimental β values for O^- photodetachment are in excellent agreement with the results of [18,19,42], but differ slightly from those of [20,28]. In addition, the present relative fine-structure transition intensity ratios are in agreement with the experimental values of [20] and confirm the effectiveness of separable geometric factors [37] for calculations of relative transition intensities, even for cases well away from threshold. Due to this separability, it is impossible to obtain experimental information on the relative partial cross sections from relative intensities alone. In contrast, the angular distributions, taken simultaneously under the same experimental conditions, are highly sensitive to the level of interference between the competing outgoing partial waves and insensitive to the geometric factors. In fact, it is the cancellation of the geometric factors, which appear in both the numerator and denominator of the Cooper-Zare formula [28], which ensures that the β values are fine-structure independent (apart from the very small energy dependence due to the multiplet splitting), as observed experimentally.

ACKNOWLEDGMENTS

This research was supported by Australian Research Council Discovery Project Grants No. DP04051253 and

DP0666267. The authors are indebted to J. R. Gascooke for discussions on the use of image morphing and Abel inversion software. The authors are also grateful to A. R. P. Rau for extensive discussions on atomic photodetachment theory.

-
- [1] D. W. Chandler and P. L. Houston, *J. Chem. Phys.* **87**, 1445 (1987).
- [2] A. T. J. B. Eppink and D. H. Parker, *Rev. Sci. Instrum.* **68**, 3477 (1997).
- [3] E. W. Hansen and P.-L. Law, *J. Opt. Soc. Am. A* **2**, 510 (1985).
- [4] V. Dribinski, A. Ossadtchi, V. Mandelshtam and H. Reisler, *Rev. Sci. Instrum.* **73**, 2634 (2002).
- [5] M. J. J. Vrakking, *Rev. Sci. Instrum.* **72**, 4084 (2001).
- [6] A. T. J. B. Eppink, S.-M. Wu, and B. J. Whitaker, in *Imaging in Molecular Dynamics, Technology and Applications*, edited by B. J. Whitaker (Cambridge University Press, Cambridge, UK, 2003), Chap. 3.
- [7] C. R. Gebhardt, T. P. Rakitzis, P. C. Samartzis, V. Ladopoulos, and T. N. Kitsopoulos, *Rev. Sci. Instrum.* **72**, 3848 (2001).
- [8] D. Townsend, M. Minitti, and A. Suits, *Rev. Sci. Instrum.* **74**, 2530 (2003).
- [9] J. Lin, J. Zhou, W. Shiu, and K. Lin, *Rev. Sci. Instrum.* **74**, 2495 (2003).
- [10] B. Bagueard, J. B. Wills, F. Pagliarulo, F. Lépine, B. Climen, M. Barbaie, C. Clavier, M. Lebeault, and C. Bordas, *Rev. Sci. Instrum.* **75**, 324 (2004).
- [11] A. Osterwalder, M. J. Nee, J. Zhou, and D. M. Neumark, *J. Chem. Phys.* **121**, 6317 (2004).
- [12] G. J. Rathbone, T. Sanford, D. Andrews, and W. C. Lineberger, *Chem. Phys. Lett.* **401**, 570 (2005).
- [13] T. Andersen, *Phys. Rep.* **394**, 157 (2004); and references therein.
- [14] D. T. Vier and J. E. Mayer, *J. Chem. Phys.* **12**, 28 (1944); and references therein.
- [15] D. M. Neumark, K. R. Lykke, T. Andersen, and W. C. Lineberger, *Phys. Rev. A* **32**, 1890 (1985).
- [16] C. Blondel, W. Chaibi, C. Delsart, C. Drag, F. Goldfarb, and S. Kröger, *Eur. Phys. J. D* **33**, 335 (2005); and references therein.
- [17] C. Blondel, C. Delsart, C. Valli, S. Yiou, M. R. Godefroid, and S. Van Eck, *Phys. Rev. A* **64**, 052504 (2001).
- [18] J. H. Hall and M. W. Siegel, *J. Chem. Phys.* **48**, 943 (1968).
- [19] D. Hanstorp, C. Bengtsson, and D. J. Larson, *Phys. Rev. A* **40**, 670 (1989).
- [20] F. Breyer, P. Frey, and H. Hotop, *Z. Phys. A* **286**, 133 (1978).
- [21] D. L. D. Osborn, D. Cry, and D. Neumark, *J. Chem. Phys.* **104**, 5026 (1996).
- [22] C. J. Dedman, E. H. Roberts, S. T. Gibson, and B. R. Lewis, *Rev. Sci. Instrum.* **72**, 2915 (2001).
- [23] S. J. Cavanagh, E. H. Roberts, M. N. Gale, C. J. Dedman, S. T. Gibson, and B. R. Lewis, *Rev. Sci. Instrum.* (to be published).
- [24] *Simion*TM, <http://www.simion.com/>.
- [25] M. N. R. Ashfold, N. H. Nahler, A. J. Orr-Ewing, O. P. J. Vieuxmaire, R. L. Toomes, T. N. Kitsopoulos, I. A. Garcia, D. A. Chestakov, S.-M. Wu, and D. H. Parker, *Phys. Chem. Chem. Phys.* **8**, 26 (2006).
- [26] S. Manzhos and H.-P. Looock, *Comput. Phys. Commun.* **154**, 76 (2003).
- [27] E. H. Roberts, S. J. Cavanagh, S. T. Gibson, B. R. Lewis, C. J. Dedman, and G. J. Picker, *J. Electron Spectrosc. Relat. Phenom.* **144-147**, 251 (2005).
- [28] J. Cooper and R. N. Zare, *J. Chem. Phys.* **48**, 942 (1968).
- [29] P. C. Engelking and W. C. Lineberger, *Phys. Rev. A* **19**, 149 (1979).
- [30] C. E. Moore, *Tables of Spectra of Hydrogen, Carbon, Nitrogen and Oxygen* (CRC Press, Inc., Boca Raton, FL, 1993).
- [31] K. M. Ervin, I. Anusiewicz, P. Skurski, J. Simons, and W. C. Lineberger, *J. Phys. Chem. A* **107**, 8521 (2003).
- [32] E. Wigner, *Z. Phys.* **83**, 253 (1933).
- [33] A. R. P. Rau and U. Fano, *Phys. Rev. A* **4**, 1751 (1971).
- [34] W. C. Lineberger and B. W. Woodward, *Phys. Rev. Lett.* **25**, 424 (1970).
- [35] A. R. P. Rau, in *Electron and Photon Interactions with Atoms*, edited by H. Kleinpoppen and M. R. C. McDowell (Plenum, New York, 1976), Chap. 12, pp. 141–148.
- [36] D. Dill, A. F. Starace, and S. T. Manson, *Phys. Rev. A* **11**, 1596 (1975).
- [37] C. Pan and A. F. Starace, *Phys. Rev. A* **47**, 295 (1993).
- [38] J. Berkowitz and G. L. Goodman, *J. Chem. Phys.* **71**, 1754 (1979).
- [39] G. L. Goodman and J. Berkowitz, *J. Chem. Phys.* **94**, 321 (1991).
- [40] The photoelectron intensities were evaluated for 5° slices of the VM image. Smaller angular slices did not result in significantly different slopes or β parameters.
- [41] S.-M. Wu, X. Yang, and D. H. Parker, *Mol. Phys.* **103**, 1797 (2005).
- [42] O. Zatsarinny and K. Bartschat (private communication).
- [43] O. Zatsarinny and K. Bartschat, *Phys. Rev. A* **73**, 022714 (2006).
- [44] M. L. Lipciuc, J. B. Buijs, and M. H. M. Janssen, *Phys. Chem. Chem. Phys.* **8**, 219 (2006).